Ultrasonics 91 (2019) 150–160

Contents lists available at ScienceDirect

Ultrasonics

journal homepage: www.elsevier.com/locate/ultras

Diverging beam transmit through limited aperture: A method to reduce ultrasound system complexity and yet obtain better image quality at higher frame rates

B. Lokesh, Arun K. Thittai*

Biomedical Ultrasound Laboratory, Department of Applied Mechanics, Indian Institute of Technology Madras, Chennai, India

ARTICLE INFO

Keywords:
Beamforming
Diverging beam
Resolution
Synthetic aperture
Ultrasound

ABSTRACT

In this paper, a technique combining Diverging Beam with Synthetic Aperture Technique (DB-SAT) is demonstrated that utilizes only limited number of active elements yet provides better quality images at higher frame rates than possible with Conventional Focused Beamforming (CFB). The DB-SAT has been investigated in simulations and experiments on wire and tissue-mimicking phantoms, and the results are compared with routinely used CFB with Linear Array (CFB-LA). The estimated lateral resolution at the focal point was 0.41 mm and 0.34 mm for CFB-LA and DB-SAT, respectively, in simulations. These were estimated to be 0.78 mm and 0.71 mm, respectively, in experiments. Experimentally computed contrast resolution (contrast-to-noise ratio) for the cyst located at 60 mm depth were 0.50 (1.31 dB) and 0.58 (2.33 dB) for CFB-LA and DB-SAT, respectively. The frame-rate achieved by DB-SAT was 8 times and 2 times higher than that achieved by CFB-LA when transmit sub-apertures had an overlap 0% and 75%, respectively. Therefore, it can be concluded from the results that DB-SAT using 8 active transmit elements and 64 active receive elements yields better quality images at higher frame-rates than those obtained using CFB-LA with 64 active elements in transmit and receive. Since there is a reduction in the number of active transmit elements in the case of DB-SAT, it leads to a reduction in the overall system complexity.

1. Introduction

Ultrasound (US) is the second most widely used imaging modality in medical diagnostic applications due to its non-invasive, non-ionizing, and real-time imaging capabilities [32]. The two most popular techniques in US imaging are using Phased Array (PA) and Linear Array (LA), both of which employ Conventional Focused Beamforming (CFB) approach. Typically, CFB approach utilizes fixed focusing during transmission and dynamic focusing during reception. The CFB based imaging techniques are routinely used in most commercial US scanners. In PA imaging [18], all transducer elements are active during both transmission and reception. Echoes received by all the transducer elements are beamformed to obtain a single A-line. An image is formed from many such A-lines, which are obtained by focusing and steering the beam in different directions using appropriate time delays. As compared to PA imaging, LA imaging activates a group of transducer elements (i.e., active sub-aperture) to obtain a single A-line. The active sub-aperture is then electronically translated over the entire transducer aperture to obtain many such A-lines, which are then juxtaposed to form the final image. Another important difference between these two imaging techniques has to do with the type of transducer used. Typically, the array-transducer used in PA imaging has inter-element separation of $\lambda/2$ (i.e., pitch = $\lambda/2$, where λ is the operating wavelength of the transducer) while the one used in LA imaging has a pitch of λ.

Trade-offs in US imaging system involve image quality, field-of-view, frame-rate, cost and complexity of the system. The resolution of an image can be improved by increasing the frequency of the US signal, but it limits the depth of penetration. Cost and complexity of an US system are dictated by the number of parallel transmit and receive channels used during data acquisition [2]. Since PA imaging uses RF data from all the elements during beamforming, it is more complex and expensive compared to LA imaging for a given linear array footprint. Nevertheless, even a regular ultrasound LA scanner is not affordable for routine scanning in resource poor settings in developing countries [30,12,27,29]. Typical low-cost ultrasound system comes with 32 transmit and receive channels or less and use delay and sum beamforming implemented on FPGA [27]. Ultrasound systems having CFB with 64 active transmit and receive elements are regularly used in

* Corresponding author at: Biomedical Ultrasound Laboratory, Department of Applied Mechanics, Indian Institute of Technology Madras, Chennai 600036, India.
E-mail address: akthittai@iitm.ac.in (A.K. Thittai).

https://doi.org/10.1016/j.ultras.2018.08.016
Received 22 March 2018; Received in revised form 14 August 2018; Accepted 20 August 2018
Available online 21 August 2018
0041-624X/

clinical practice, and are considered to provide acceptable image quality for reliable diagnosis. Therefore, systems that can use fewer or equal number of active elements compared to that used in a low-cost system, yet provide image quality better than that obtained from routinely used systems employing 64-active elements and CFB, can be considerd as desirable.

Efforts to miniaturize the US scanner and make it more affordable has been an area of active research over the years. To reduce the system's complexity, the notion of synthetic aperture radar was adapted to medical US [3]. The Synthetic Aperture Technique (SAT) [36] makes use of only one channel to acquire data and form an image. Here, a single transducer element is activated at a time to transmit an unfocused beam and backscattered echoes are received by the same element. Likewise, all transducer elements are activated sequentially and RF data from all transmits are stored in the memory, which are then beamformed and processed to obtain the final image. This technique is less complex, but the resulting compromise in image quality has been an issue for biomedical applications. There has been a significant number of works that have tried to overcome the limitations of SAT and adapt it for biomedical imaging as detailed below.

Initial efforts were made towards utilizing the concept of SAT to reduce the complexity of the PA imaging systems [34,13,10]. These approaches generally used fewer active elements to reduce the hardware complexity at the expense of frame-rate, which sometimes compromised the real-time imaging capability. Specifically, Trahey and Nock [34] employed a technique, which uses an available number of active elements to form a single A-line and the process of image formation is same as the PA imaging. This technique retained the real-time imaging capability, however, it compromised on the image quality when compared to the full-PA imaging. Karaman et al. [13] proposed an imaging approach, which transmits a defocused beam from the subaperture (5 active elements) and echoes were received in all elements using sub-aperture multiplexing. This process was repeated by moving the transmit sub-aperture, one element at a time. Johnson et al. [10] proposed a phased subarray imaging method, where the subapertures (4 active elements) were used to focus and steer the beam in different directions to form RF images and then these were laterally upsampled, interpolated, weighted, and coherently summed to form the final image.

Several methods have been reported that exploit synthetic aperture approach for LA imaging [16,5,35]. In general, these methods have used sparse and/or Multi-element Synthetic Transmit Aperture (MSTA) to achieve higher frame-rates and/or better image quality when compared to LA imaging. However, in order to retain frame rates without sacrificing possible image quality, these techniques utilized active elements over the full-receive aperture leading to a hardware-wise complex and expensive system. Recently, a 2R-SAT has been proposed for less complex US system with LA transducer that uses only two channels during data acquisition [19]. Data acquisition is similar to the SAT, but only two elements are used to receive the echoes. This technique, when used with the coded-excitation on transmit, was shown to yield significantly better signal-to-noise ratio (SNR) and depth of penetration when compared to the traditional SAT. However, the frame-rate is only comparable to those achievable in CFB-approaches.

In addition to the above efforts, recent developments in ultrasound modality have aimed at achieving very high frame-rate imaging ($>$ 1000 fps). This is achieved using plane-wave transmit or diverging waves with a virtual source behind the transducer [21,8,24]. Further, compounded plane waves or diverging waves are used to improve the contrast and resolution. Here, plane waves or diverging waves are steered in different directions and spatial compounding approach is used to obtain a final image. However, these methods require high channel count in transmission and reception, thus leading to very sophisticated and complex systems. Recently, another method was developed by Gong et al. [6] to achieve a very high frame-rate system using sub-apertures in a linear array to emit diverging beam. Even though it uses subaperture, it still involves excitation of all transducer elements simultaneously as is done in plane wave imaging.

In summary, although a number of techniques have been investigated and reported in the literature that exploit STA approach, none have explicitly investigated a combination of diverging beam and SA with sparse transmit and sparse receive for LA imaging. Almost all of the prior works utilized diverging beams with an aim to achieve high frame-rate or to improve lateral resolution without worrying about complexity of the system. In this work, we propose a technique that combines Diverging Beam with Synthetic Aperture Technique (DB-SAT) for LA imaging to provide less complex system, which uses only one 8-channel pulser IC, having superior lateral resolution and higher frame-rates than CFB-based LA imaging. This is accomplished by employing a sparse, multi-element transmission of diverging waves and performing SA beamforming. Further, we have investigated the effects of a reduction in the number of active receive elements on the image quality. Specifically, we have calculated and compared the frame rate, contrast, axial resolution, and lateral resolution obtained from CFB with Linear Array (CFB-LA) and DB-SAT.

This paper is organized as follows. The DB-SAT is presented in Section 2 along with the beamforming algorithm and methods used in simulation and experiment. Section 3 presents results from the simulation, experimental validation of simulation results, and comparison of example in-vivo image obtained using the CFB-LA and DB-SAT. Discussion and conclusions based on this work are reported in Section 4.

2. Materials and methods

2.1. Diverging beam with synthetic aperture technique (DB-SAT)

The DB-SAT imaging sequence is shown in Fig. 1. During transmit, a diverging beam is sent out from the active elements (N_A = 8) of the transducer array by supplying appropriate delay values. The backscattered echoes are received by active receive elements of the transducer array and stored for further processing. This process is continued by electronically translating the active transmit sub-aperture with or without an overlap, until all the transducer elements are used. The location of active receive elements is chosen based on the position of the virtual source, for example, the active receive elements for the 8th emission (transmit active elements located at 57–64) is shown in Fig. 1. For each transmission from the sub-aperture, the echoes received by the active receive elements (pre-beamformed RF data) are stored separately. The stored data are beamformed using Delay and Sum (DAS)

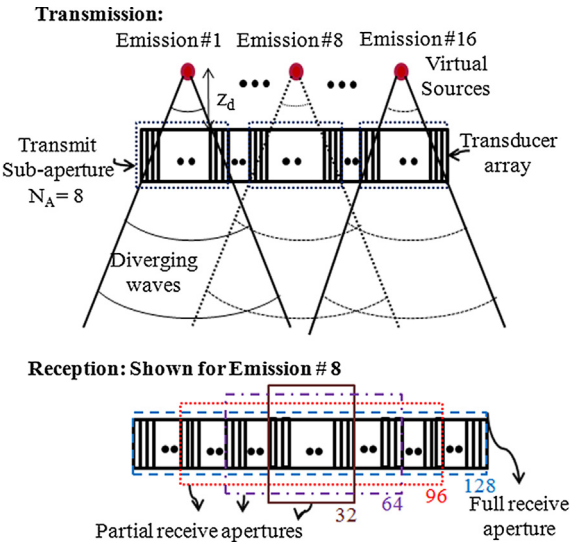

Fig. 1. A sketch depicting the transmit-receive sequence in DB-SAT without overlap of transmit sub-aperture.

algorithm, which is explained a few paragraphs below from here.

Note, the choice of using 8 active elements during transmit in this study is mainly because of the following two reasons.

1. Increase in the size of the transmit sub-aperture (i.e., particularly more than 16 elements) leads to a degradation in the image quality due to axial lobes, which was previously reported by many authors [13,26,17].
2. Ready availability of 8-channel HV-Pulser IC module, which is state of the art [23,7].

Delay values that are used to activate transducer elements to emit a diverging beam are computed using (1), which was previously reported in the literature [13,26]. The number of virtual sources and the inter-spacing of the virtual sources depend on the overlapping of transmit sub-aperture that is used to obtain the final image. A systematic evaluation of the influence of these parameters on the image quality is reported in Section 3.4 later.

$$\tau_n = \frac{x_n^2}{2cz_d} \tag{1}$$

where, x_n is the distance of the n^{th} element from the center of the transmit sub-aperture, and d is the inter-element spacing, and c is the speed of sound.

In this study, z_d is chosen as $dN_A/2$, is the distance from the virtual source to the transducer array, which is 1.2 mm to produce a transmit beam as wide as the full sector image (i.e., beam divergence angle = 90°). A thorough investigation of virtual source distance from the transducer array on image quality metrics is reported in Appendix A.

The stored pre-beamformed RF data are processed using the DAS algorithm to form post-beamformed RF data. DAS beamforming is performed at each point 'p' in the raw RF data using (2).

$$S(p) = \sum_{i=1}^{N_e} \sum_{j=1}^{N_{rx}} w_{ij} RF_{ij}(t-\tau) \tag{2}$$

$$\tau = [\sqrt{((z_f + z_d)^2 + (x_f + x_i)^2)} + \sqrt{(z_f{}^2 + (x_f + x_i)^2)}]/c \tag{3}$$

where RF_{ij} represents RF data, obtained using i^{th} emission from transmit sub-aperture and reception from the j^{th} element, N_e and N_{rx} represents the number of emissions from transmit sub-aperture and number of receive elements, respectively, (x_f, z_f) is the focus point in the image, τ represents time taken from the virtual source to the focus point and back to the receive element, and w_{ij} represents the corresponding apodization weights.

2.2. Field II simulations

Simulations were done using Field II® software [9]. Linear array transducer was modeled separately for CFB-LA and DB-SAT with acquisition parameters as listed in Table 1. To obtain CFB-LA RF data, the active aperture (i.e., 64 elements) was made to focus the beam at 40 mm depth by incorporating appropriate time-delays. Echoes were received from the same active aperture and then beamformed using dynamic receive focusing (with dynamic aperture having F-number = 2) to obtain single A-line. This transmit-receive process was repeated to acquire 128 A-lines by electronically translating the active aperture one element at a time. All these A-lines were then populated next to each other to obtain the final image. In DB-SAT, pre-beamformed RF data were collected and beamformed using the aperture containing the active receive elements. To study the effect of the number of active receive elements used in beamforming, it was varied as 128, 96, 64, and 32. However, to reduce the near field clutter, a dynamic aperture (with F-number = 2) was used until the number of active receive elements were reached. B-mode images were formed by applying band-pass filtering, envelope detection and log compression on the beamformed RF data [1]. The dynamic range of the images was set to 60 dB in simulations.

Table 1
Transducer parameters used in field II simulation.

Parameters	DB-SAT	CFB-LA
Number of elements (N)	128	128
Transmit Active elements (N_A)	8	64
Inter-element spacing	0.3 mm	0.3 mm
Element width	0.275 mm	0.275 mm
Element height	4 mm	4 mm
Centre frequency	5 MHz	5 MHz
Sampling frequency	40 MHz	40 MHz
Transducer-Phantom spacing (z-start)	5 mm	5 mm

A computer phantom was simulated that contained 30 point-scatterers arranged in 3 columns, each column having 10 point-scatterers. The point scatterers were separated by a distance of 10 mm both in the axial and lateral directions. This computer-generated phantom was imaged separately using the CFB-LA and DB-SAT. Axial and lateral resolutions at different depths were estimated using the full width at half maximum (FWHM) (−6 dB) value obtained from the axial and lateral profile of the scatterer at that depth, respectively. Further, the improvements in depth of penetration of DB-SAT by increasing the amplitude of the excitation signal were also investigated. To study this, a computer phantom that was simulated by incorporating an attenuation coefficient value of 0.5 dB/[cm MHz] was used. The amplitude of the excitation signal was increased from 15.7 to 48.6 V (~3 times), which was the maximum realizable in the SONIX TOUCH Q+ US scanner (refer to Table V4 in the manual, page no. 247) used in experimental validation. Note that unlike CFB, we employ diverging beam and this perhaps provides an opportunity for increasing the amplitude of the excitation signal without possibly worrying about the biosafety aspects. Nevertheless, the scope of the work reported in this paper is just to explore this possibility. Some additional discussions are made in the last section.

In order to analyze the image contrast, a computer cyst phantom was simulated with dimensions 70 mm × 40 mm × 5 mm (height x width × length), that contained cysts of different sizes and also hyperechoic regions. Cyst phantom image for both techniques were obtained by repeating the data acquisition process in the same way as described before. The attenuation was set to 0.5 dB/[cm MHz]. To make simulations more realistic, white Gaussian noise was added to the simulated RF data corresponding to a SNR of 40 dB.

In order to compare the image contrast performance of different techniques, Contrast Resolution (CR) and contrast-to-noise ratio (CNR) were estimated for cysts present on the right side in the image by taking a 3 mm × 3 mm region of interest. The CR and CNR were calculated using (4) and (5), respectively [25].

$$CR = \frac{(s_{out} - s_{in})}{s_{out}} \tag{4}$$

$$CNR = 20log10\frac{|s_{out} - s_{in}|}{\sqrt{(\sigma_{in}^2 + \sigma_{out}^2)}} \tag{5}$$

where s_{in} and s_{out} are the mean values of target and background, respectively, and σ_{in} and σ_{out} are the corresponding standard deviations.

2.3. Experiments

Experiments were performed using SONIX TOUCH Q+® US scanner (Ultrasonix, Analogic Corporation, Peabody, MA, USA). A 128-element linear array transducer (L14-5/38) operating at a center frequency of 5 MHz and a sampling frequency of 40 MHz was used for this purpose. In the case of CFB-LA, post-beamformed RF data were acquired by setting the transmit focus to 40 mm. In the case of DB-SAT, pre-

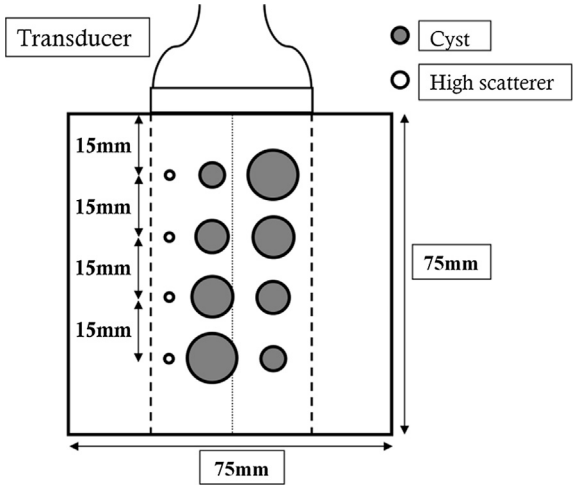

Fig. 2. A cross-sectional view of the tissue-mimicking phantom model that was used in experiments. The phantom geometry, along with dimensions, is described.

beamformed RF data were acquired and beamformed using DAS algorithm as explained in simulation section. The estimation of lateral resolution, axial resolution, and formation of B-mode images were similar to what was explained in the simulation section. The dynamic range of the images was set to 60 dB in experiments as well.

To validate the results obtained from a simulated point scatterer phantom, a wire phantom was constructed and imaged. This phantom was made using a set of 16 wires made of Nylon having a diameter of 0.36 mm each. The wires were arranged in two columns, each having 8 wires separated by 10 mm laterally and axially. This complete setup was immersed in a water bath and the cross-section of the wires were imaged. The axial and lateral resolution values were computed from the 8 wires positioned at different depths and located at 5 mm in the lateral direction.

The image contrast was assessed in experiments on a tissue-mimicking phantom that was made using agar-gelatin-water mixtures [11]. The phantom had overall dimensions 75 mm × 75 mm × 75 mm (height x width × length), that contained cysts of different sizes and regions with high scatterer density, which ran along the length of the phantom. The phantom cross-section view is shown in Fig. 2. To manufacture this phantom, a cuboid-shaped mold was made using polypropylene with a provision for inserting different-sized cylinders at different positions. The phantom material was prepared by mixing 5% by the weight of gelatin and 4% by the weight of agar with deionized water at 80 °C and was stirred well until the temperature came down to about 30 °C. Thereafter, this mixture was poured into the mold with the cylindrical inserts in place and allowed to cool at 4 °C for approximately 12 hrs. Later, the cylindrical inserts were carefully removed. To obtain the high scattering regions, nylon wires, having a diameter of 1 mm were inserted into the holes present in the phantom.

In order to explore and understand the potential of the DB-SAT further, RF data were collected from right-hand biceps of a 28-year old male volunteer using CFB-LA and DB-SAT, and were beamformed separately. Thereafter, B-mode images were formed in a similar way as explained earlier in the simulation section.

3. Results

3.1. Point scatterer imaging

Fig. 3 shows B-mode images of the computer phantom obtained using CFB-LA and DB-SAT with different number of active receive elements. It can be readily observed that the DB-SAT provides depth independent lateral resolution for all cases considered, except for 32 receive elements. However, the lateral resolution obtained using 32 receive elements is still comparable to that obtained using CFB-LA. It can also be noticed that the images obtained using DB-SAT are noisier when compared to that obtained from CFB-LA. Fig. 4 depicts the plot of the axial and lateral resolutions, estimated as the FWHM from point scatterers located at different depths in the image (center column), obtained by CFB-LA and DB-SAT using various number of active receive elements. In the case of CFB-LA, the lateral resolution value increases significantly beyond the focal depth (i.e., 40 mm), indicating poorer resolution as we can see in Fig. 4(a). On the other hand, DB-SAT with active receive elements greater than 64 maintains the improved resolution throughout the depth. For example, at 80 mm depth, the lateral resolution of the DB-SAT shows about 4 times improvement over that obtained in the CFB-LA. On the other hand, one can see from Fig. 4(b) that the axial resolution is almost same for all the techniques at all depths. Notice the abrupt change in the axial resolution at larger depths in the case of DB-SAT with 32 receive elements. This is due to the loss in energy of the main lobe signal at larger depths, which resulted in the amplitude of the axial lobes [26,28] comparable to that of main lobes and affected the calculation of axial resolution.

Fig. 5 compares the B-mode images of the computer phantom obtained using CFB-LA and DB-SAT with full receive aperture at two

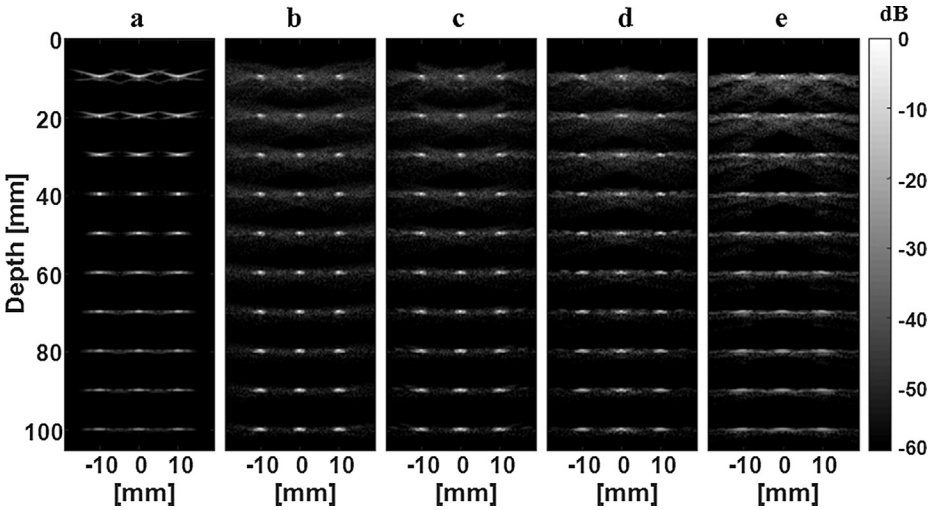

Fig. 3. Simulated B-mode images of phantom containing 30 point-scatterers obtained using (a) CFB-LA, and DB-SAT for different active receive elements, (b) 128, (c) 96, (d) 64, and (e) 32.

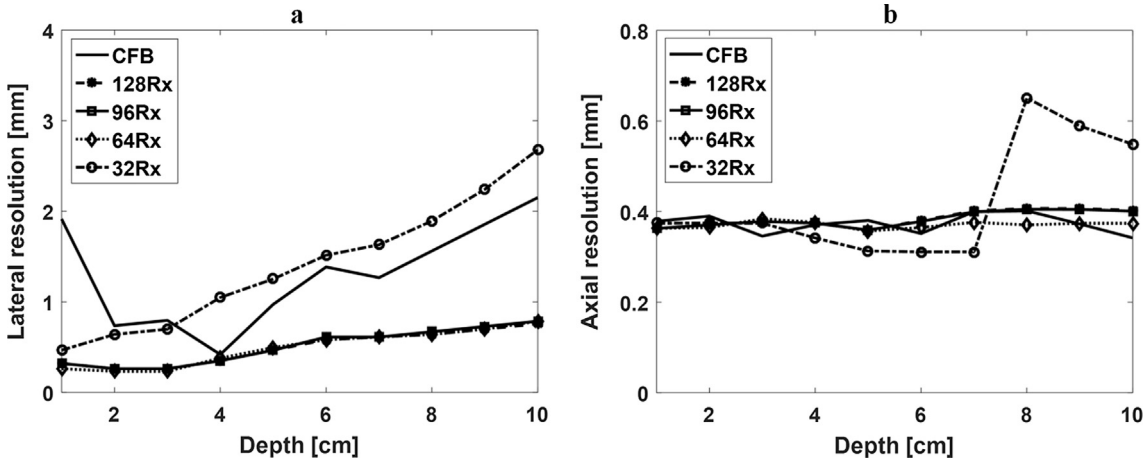

Fig. 4. Plots of the estimated (a) lateral resolution and (b) axial resolution at different depths obtained in simulations when using different methods, i.e., CFB-LA, DB-SAT with various active receive elements. The results were obtained from point scatterers positioned at 0 mm lateral location.

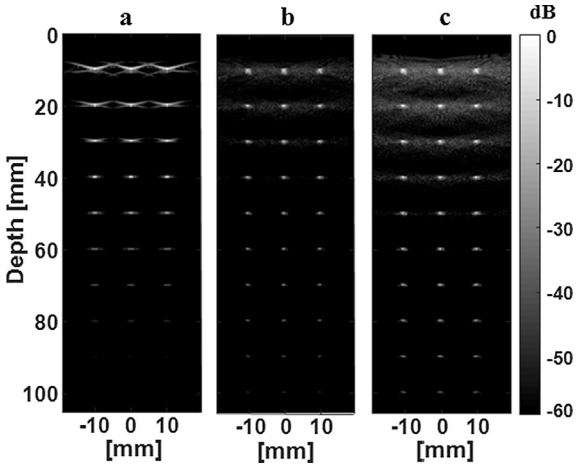

Fig. 5. Simulated B-mode images of a phantom containing 30 point-scatterers obtained using (a) CFB-LA, (b) DB-SAT with full receive aperture and (c) DB-SAT with full receive aperture, but the excitation signal is 3 times of that used in (b). The attenuation was set to 0.5 dB/[cm MHz].

different transmit pulse amplitude settings. One can notice that the scatterers located beyond 60 mm are not visible in the image obtained using CFB-LA, whereas they are visible in the images obtained using DB-SAT. As would be expected, the visibility of the scatterers is more prominent when the amplitude of the excitation signal is increased. Fig. 6 compares the normalized lateral profile obtained by taking the cross section at 60 mm depth of the images shown in Fig. 5. In DB-SAT, the amplitude of received echo is improved by about 10 dB when the excitation signal is increased by 3 times.

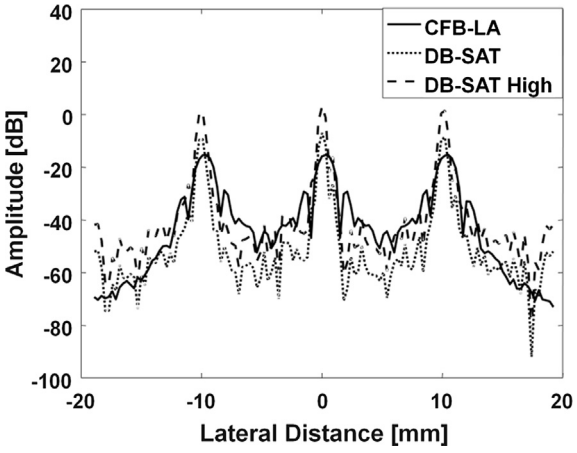

Fig. 6. Plots of normalized lateral profile obtained at 60 mm taken from point-scatterers images obtained in simulations when using CFB-LA, DB-SAT with full receive aperture having excitation signal that is same as CFB-LA and 3 times (DB-SAT High) greater than what was used in CFB-LA.

3.2. Computer cyst phantom

Fig. 7 shows B-mode images of the computer cyst phantom obtained using CFB-LA and DB-SAT with different number of active receive elements. Although subtle, one can notice that the shape of the cyst is distorted in the case of CFB-LA (observe that the cyst is slightly elliptical, which is prominent in the deeper seated cysts), whereas it is retained in DB-SAT images. However, the image obtained using DB-SAT with 32 receive elements is poor compared to those obtained with other active receive elements. The CR and CNR values calculated from the images shown in Fig. 7 are summarized in Table 2. The letter 'R' refers to the cysts present on the right side in the image. These values obtained from cysts present in CFB-LA images are larger when compared to DB-SAT using different number of active receive elements.

3.3. Wire phantom

Fig. 8 presents the B-mode images obtained in experiments performed on the wire phantom. The experimental results corroborate with the simulation results shown in Fig. 3. DB-SAT demonstrates an improvement in the lateral resolution for all active receive elements, except the one containing 32 receive elements. The improvement was quantified in terms of estimated lateral resolution values (i.e., FWHM) as shown in Fig. 9(a). Clearly, the DB-SAT provides better lateral resolution than that obtained from CFB-LA due to the dynamic focusing during both transmission and reception. The lateral resolution obtained using CFB-LA deteriorates significantly after the focus point as we observed in simulations. The plot of the axial resolution obtained using CFB-LA and DB-SAT with various active receive elements is shown in Fig. 9(b). The obtained axial resolution is comparable between CFB-LA and DB-SAT with different active receive elements, which is consistent with what we have observed in the simulation.

Fig. 10 compares the B-mode images obtained in experiments performed on the wire phantom using CFB-LA and DB-SAT with full receive aperture at different amplitude of the pulser excitation signal. One can clearly notice that the brightness of the point scatterers are increased, when the amplitude of the excitation signal was increased, which is quantified in Fig. 11 that compares the normalized lateral profile taken at 60 mm depth of the images shown in Fig. 10. The

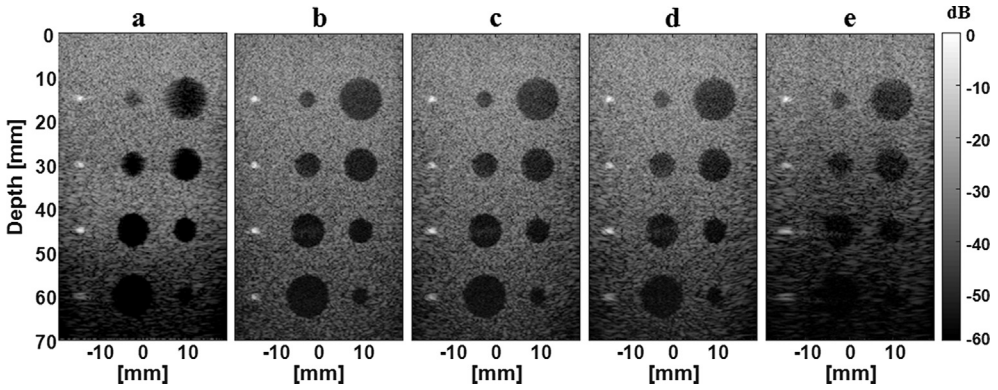

Fig. 7. Simulated B-mode images of cyst phantom obtained using (a) CFB-LA, DB-SAT for different active receive elements, (b) 128, (c) 96, (d) 64, and (e) 32. The attenuation was set to 0.5 dB/[cm MHz].

Table 2
Calculated CR and CNR values for simulated cyst phantoms.

	CFB-LA		DB-SAT (128 Rx)		DB-SAT (96 Rx)		DB-SAT (64 Rx)		DB-SAT (32 Rx)	
	CR	CNR(dB)	CR	CNR(dB)	CR	CNR(dB)	CR	CNR(dB)	CR	CNR(dB)
R1	0.9667	14.9758	0.9161	11.6863	0.9074	11.6061	0.9106	11.2332	0.8790	11.0737
R2	0.9858	16.6595	0.9124	11.4547	0.9033	11.3260	0.8984	11.0250	0.7768	7.2132
R3	0.9816	17.0902	0.9237	12.6838	0.9178	12.1111	0.9040	12.1937	0.7766	9.1498
R4	0.7256	6.7309	0.7753	7.8068	0.7707	7.3541	0.7401	5.6351	0.5046	1.3188

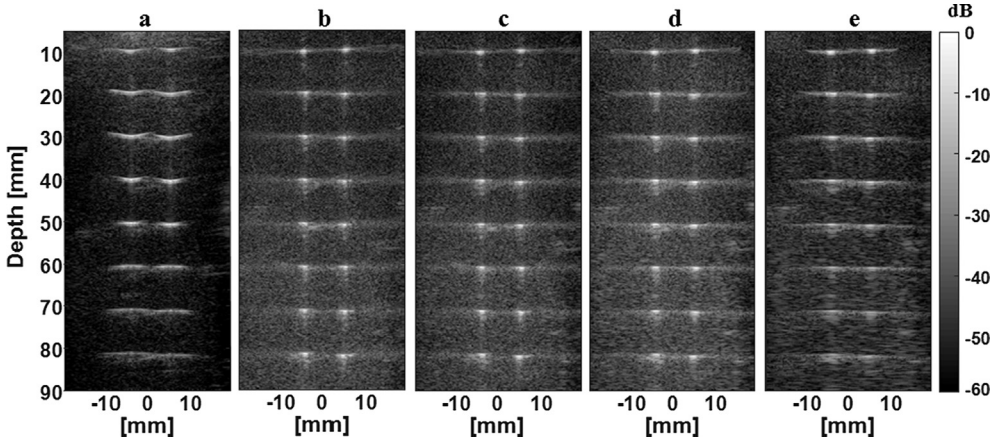

Fig. 8. B-mode images of a phantom containing 30 point-scatterers obtained in experiments using (a) CFB-LA, DB-SAT for different active receive elements, (b) 128, (c) 96, (d) 64, and (e) 32.

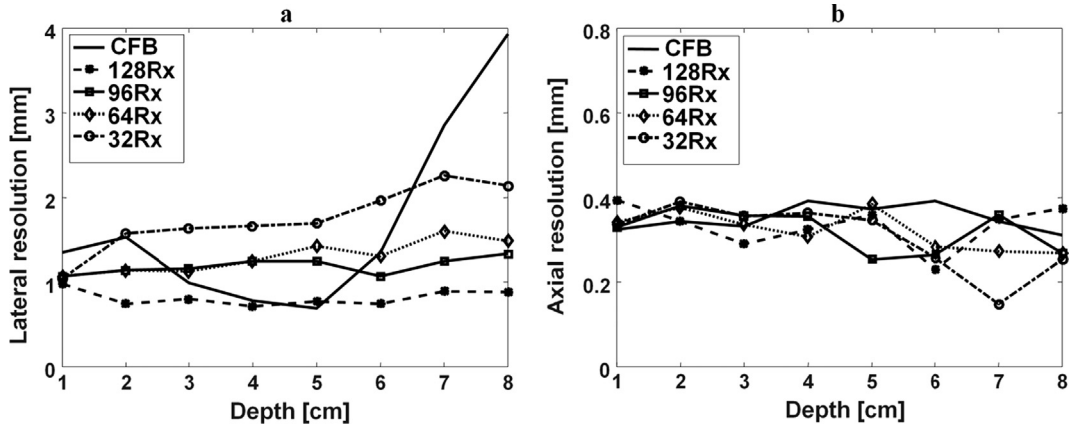

Fig. 9. Plots of the estimated (a) lateral resolution and (b) axial resolution at different depths obtained in experiments when using different methods, i.e., CFB-LA, DB-SAT with various active receive elements. The results were obtained from point scatterers positioned at 5 mm lateral location.

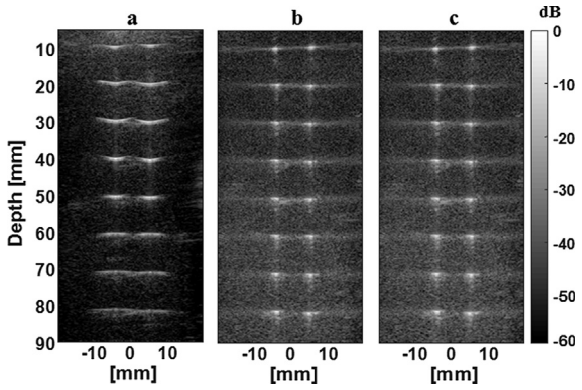

Fig. 10. B-mode images of a wire phantom obtained in experiments using (a) CFB-LA, (b) DB-SAT with full receive aperture and (c) DB-SAT with full receive aperture, but the excitation signal is 3 times of that used in (b).

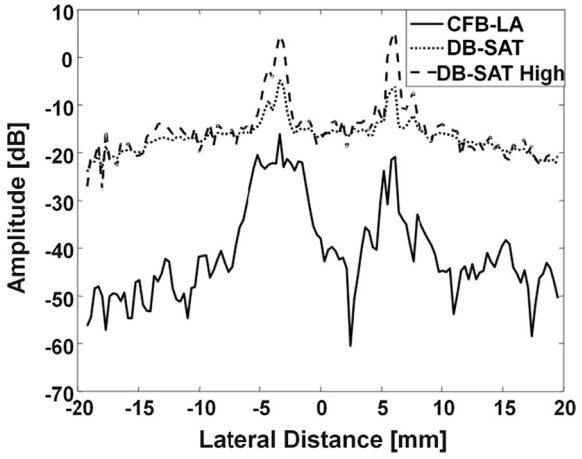

Fig. 11. Plots of the normalized lateral profile at 60 mm depth taken from wire phantom images obtained in experiment when using CFB-LA, DB-SAT with full receive aperture having excitation signal that is same as CFB-LA and when DB-SAT that employed excitation signal amplitude that was 3 times greater than what was used in CFB-LA (DB-SAT High).

amplitude of the received echo obtained using DB-SAT improved by about 11 dB compared to that obtained from the CFB-LA when same excitation signal was used. The amplitude of the received echo improved further (21 dB compared to CFB-LA), when the excitation voltage signal was increased by 3 times.

3.4. Tissue-mimicking phantom

Fig. 12 shows B-mode images of a tissue-mimicking phantom obtained using CFB-LA and DB-SAT with various number of active receive elements. As described earlier, the amplitude of excitation signal used in the case of DB-SAT was 3 times that of CFB-LA. One can notice that the B-mode image obtained from CFB-LA provides slightly better contrast than that obtained by DB-SAT. This is due to the presence of slightly-higher levels of side lobes in the case of DB-SAT than in the case of CFB-LA. Further, one can observe that the “points with high scattering” are having same spread at all depths in the images obtained using DB-SAT when compared to that obtained from CFB-LA. Interestingly, an improvement in the contrast with reduction in the number of active receive elements was observed in experiments, which is opposite to what we observed in simulations.

Furthermore, notice the appearance of vertical dark streaks in the images of a tissue-mimicking phantom obtained using DB-SAT. This is possibly due to lack of transmit aperture overlap in sparse scheme employed during transmit. In order to validate this, we used 25%, 50%, and 75% sub-aperture overlapping during transmit, while fixing the receive aperture (for example, $N_{rx} = 64$). Fig. 13 shows the B-mode images obtained using CFB-LA, DB-SAT without overlap and with various transmit sub-aperture overlaps. In the case of DB-SAT, we can readily observe that the vertical dark streaks are reduced as the overlap of the sub-aperture is increased. The reduction in the vertical dark streaks is quantified using Normalized Fourier Spectrum, which is shown in Fig. 14. The spectrum was estimated from an average of 10 lateral profiles taken at a depth of around 4 mm. It can be noticed that the prominent frequency spikes corresponding to the vertical streak artifact are reduced as the overlapping of transmit sub-aperture is increased. The CR and CNR values calculated from cysts present on the right side in the images shown in Fig. 13 are summarized in Table 3. It can be observed that overall the CR and CNR values are comparable between that obtained using CFB-LA and DB-SAT, but the latter yields better contrast values for the case of 75% transmit sub-aperture overlap, especially, at 60 mm depth.

3.5. In-vivo example

Fig. 15 shows B-mode images of biceps obtained using CFB-LA and DB-SAT. The DB-SAT setting had a transmit sub-aperture overlap of 75% for different number of active receive elements. The B-mode images obtained using the different receive aperture settings seem visibly comparable to that obtained using CFB-LA.

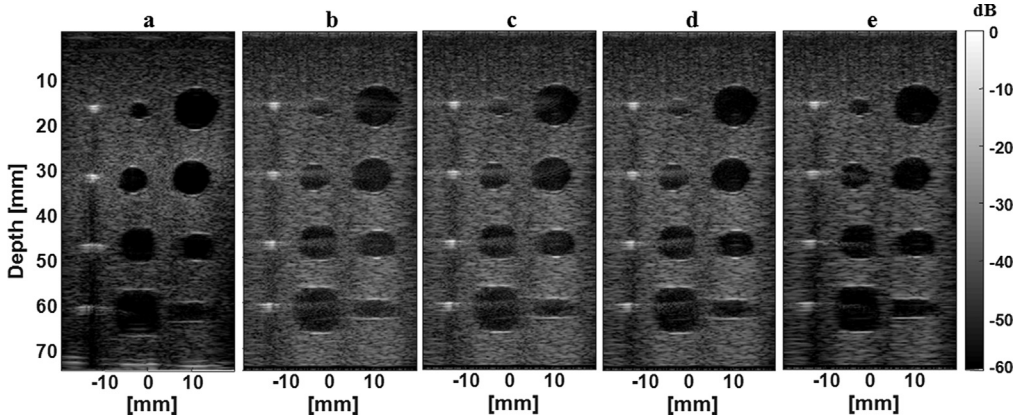

Fig. 12. B-mode images of a tissue-mimicking phantom obtained in experiments using (a) CFB-LA, DB-SAT for different active receive elements, (b) 128, (c) 96, (d) 64, and (e) 32.

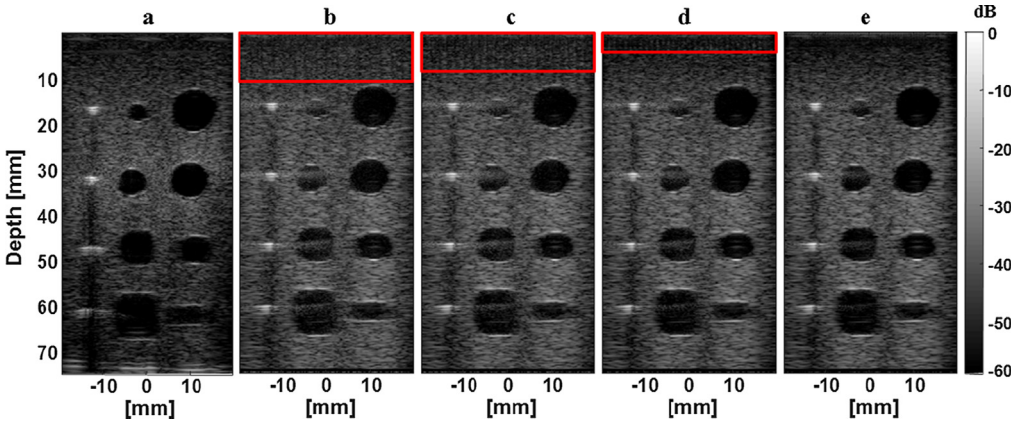

Fig. 13. B-mode images of a tissue-mimicking phantom obtained in experiments using (a) CFB-LA, DB-SAT with 64 active receive elements, (b) without an overlap, (c) 25% overlap, (d) 50% overlap, and (e) 75% overlap. One can notice vertical dark streaks prominently within the region inside the red boxes. (For interpretation of the references to colour in this figure legend, the reader is referred to the web version of this article.)

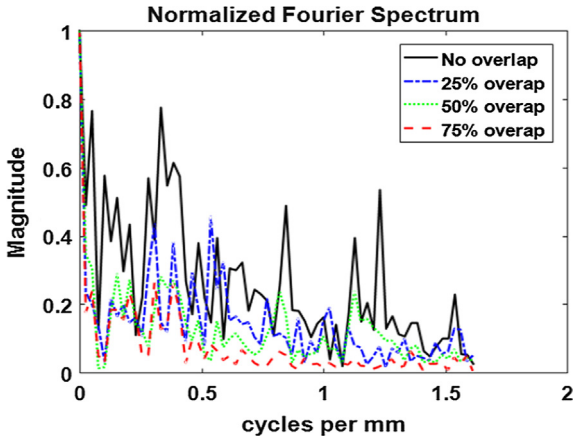

Fig. 14. Plot of the estimated normalized spectrum of an average of 10 lateral profiles taken at a depth of around 4 mm for images obtained with different overlaps.

3.6. Comparison of frame rate

Frame rate was calculated and compared among the CFB-LA and DB-SAT techniques. Table 4 presents the frame rate obtained from CFB-LA and DB-SAT with different transmit sub-aperture overlap. The theoretical frame-rate was computed using (6)

$$Frame\ rate <= \frac{c}{2zN_e} \tag{6}$$

where N_e is the number of emissions to obtain 128 A-lines, z is the depth of imaging, which was set to 80 mm, and c is the speed of sound (1540 m/s).

The frame rate achieved using DB-SAT without overlap is 8 times higher than that obtained using CFB-LA with a single focus. Even with a sub-aperture overlap of 75%, DB-SAT provides a better frame-rate than CFB-LA. In general, for imaging larger depths CFB-LA employs multiple focal zones, which decreases the frame rate by a factor equal to the number of focal zones. However, this is not the case with DB-SAT since all the points are focused during the reconstruction. Therefore, the

Table 3
CR and CNR values for images obtained in experiments.

	CFB-LA		DB-SAT (No overlap)		DB-SAT (25%)		DB-SAT (50%)		DB-SAT (75%)	
	CR	CNR(dB)	CR	CNR(dB)	CR	CNR(dB)	CR	CNR(dB)	CR	CNR(dB)
R1	0.9184	12.3663	0.8961	10.8249	0.8976	11.0361	0.9154	11.68529	0.9340	12.6147
R2	0.9501	13.4305	0.8953	10.8704	0.8975	11.41374	0.9153	11.5272	0.9269	12.1557
R3	0.8388	10.0283	0.8023	8.8395	0.8026	8.7140	0.8190	9.2874	0.8200	9.4645
R4	0.5093	1.3193	0.5862	2.3396	0.5962	2.5565	0.6019	2.7706	0.5978	2.7564

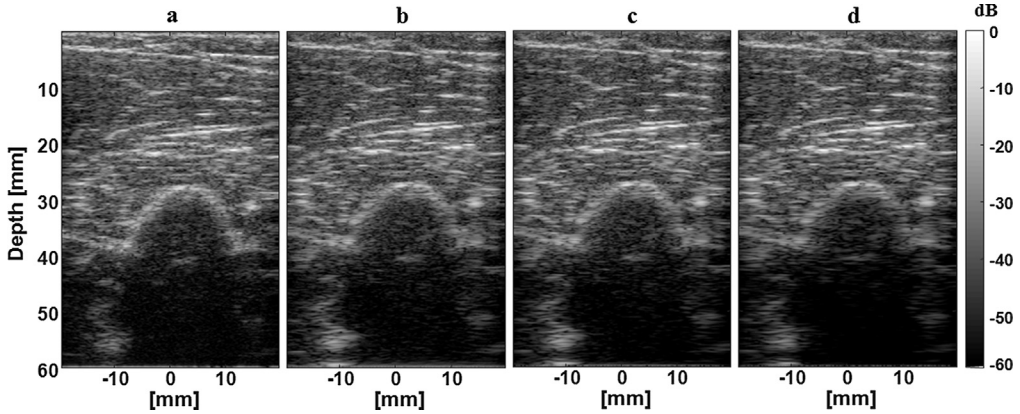

Fig. 15. In-vivo images of biceps obtained using (a) CFB-LA, DB-SAT with 75% transmit sub-aperture overlap for different active receive elements, (b) 128, (c) 64, and (d) 32.

Table 4
Theoretical frame-rate achieved by CFB-LA and DB-SAT with various transmit sub-aperture overlap.

Technique	Frame rate
CFB-LA	75
DB-SAT without overlap	601
DB-SAT with 25% overlap	458
DB-SAT with 50% overlap	310
DB-SAT with 75% overlap	158

frame-rate improvements using DB-SAT will be even higher compared to when CFB-LA employs multiple focal zones.

4. Discussion and conclusion

In this paper, a technique combining the diverging beam transmit through limited number of active elements and SAT has been proposed. The proposed DB-SAT is shown to yield better lateral resolution throughout the depth, both in simulations and experiments, unlike CFB-LA which has the best resolution only at the focus. These characteristics are achieved by the DB-SAT using only 8 active elements during transmit, thus paving a way for a less complex system design compared to the CFB-LA. In addition to this, the DB-SAT achieves higher frame rate than that achieved by CFB-LA for various transmit sub-aperture overlaps.

In the study of number of active receive elements used in beamforming, a major discrepancy was found between simulation and experimental results when using cyst phantom. It was observed that reducing the number of active receive elements tended to reduce the contrast in simulations, whereas, an improvement was noticed in experiments. This is due to the differences in the homogeneity of the insonification experienced by the simulated and experimental phantom, respectively, as shown in Fig. 16. This difference may be due to the dissimilarity between the attenuation characteristics of the simulated and actual phantom. It may also be due to the differences in element directivity of the simulated transducer to that of the actual transducer. Nevertheless, this leads to reduced clutter when using a smaller number of active receive elements in the case of experiments.

The image quality can be further improved by incorporating adaptive weighting during beamforming. Several adaptive weighting methods such as generalized coherence factor, phase coherence factor, minimum variance beamforming, etc., have been reported in literature to improve the quality of an ultrasound image [15,4,31]. Specifically, we had investigated and reported on further improvement in lateral resolution by incorporating a simple Sign Coherence Factor (SCF) weighting during beamforming [17].

Even though we investigated increasing the amplitude of the excitation signal in the case of DB-SAT to increase the SNR and depth of imaging, it has an upper limit due to the safety of patient as well as the transducer. There are several works reported in the literature to increase SNR and depth of imaging by using coded excitation during the transmission without increasing the amplitude or length of the excitation signal [22,20,14]. The Golay and Barker encoding are the widely used methods, but they compromise in the frame-rate. Other methods like chirp excitation may require changes to the pulser-side hardware. The recently introduced coded excitation sequences, for example, Hadamard, was shown to improve SNR and depth of imaging in Plane wave/diverging wave imaging without sacrificing the frame-rate [33,6,37]. The methods like Hadamard encoding can be used in DB-SAT to further increase SNR and the depth of imaging without additional hardware and without sacrificing the frame-rate.

To summarize, we proposed a technique that combines diverging beam using limited number of transmit elements with Synthetic Aperture Technique for Linear array imaging. The investigations through simulations, experiments on phantoms, and in-vivo example demonstrated that DB-SAT provides improved lateral resolution at higher frame rates when compared to the routinely used CFB-LA. Although the concepts of the diverging beam and synthetic transmit aperture themselves are well studied in literature combining them in a manner to achieve a reduction in the complexity, yet obtain better quality images at improved frame rate is novel and significant, especially, for the development of affordable scanners for resource-poor countries.

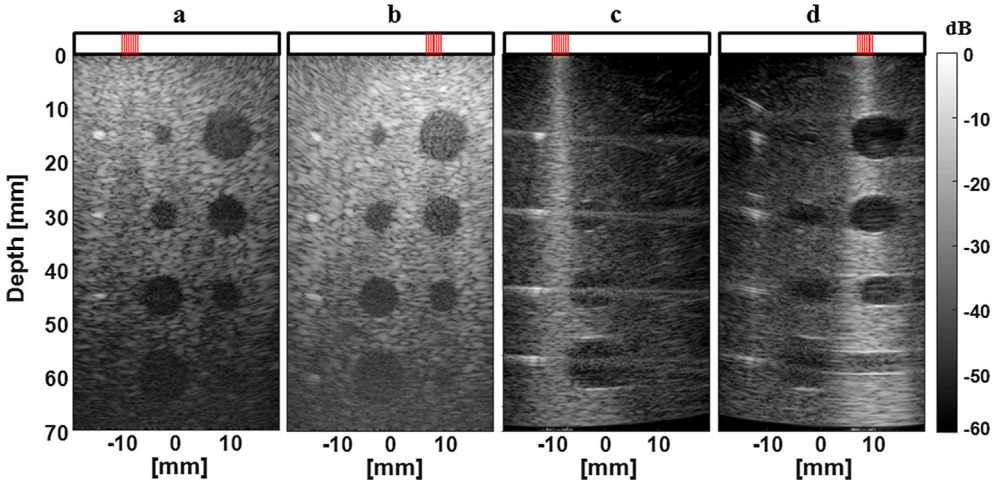

Fig. 16. Two low resolution B-mode images obtained in simulations (a&b) and experiments (c&d) using DB-SAT for the two transmit locations, active transmit elements located at 33–40 (a&c), and 89–96 (b&d), respectively, are shown.

Acknowledgements

The author Lokesh B would like to thank the Ministry of Human Resource Development (MHRD), Government of India, for financially supporting through HTRA stipend.

Appendix A. Analysis of virtual source distance from the transducer array on image quality metrics using simulations

The analysis of virtual source distance from the transducer array (z_d) on the image quality metrics is presented here. The value of z_d was varied as 1.2 mm, 2.9 mm, 4.5 mm, and 0 mm, which corresponds to beam divergence angle of 90°, 45°, 30°, and 0°, respectively. It can be observed from Fig. A1 that the lateral resolution improves and the contrast decreases as the value of z_d decreases. Thus, there is a trade-off between the lateral resolution and contrast of an image as the value of z_d is changed. Notice that both lateral resolution and contrast resolution are poor in the case of unfocused beam i.e., $z_d = 0$.

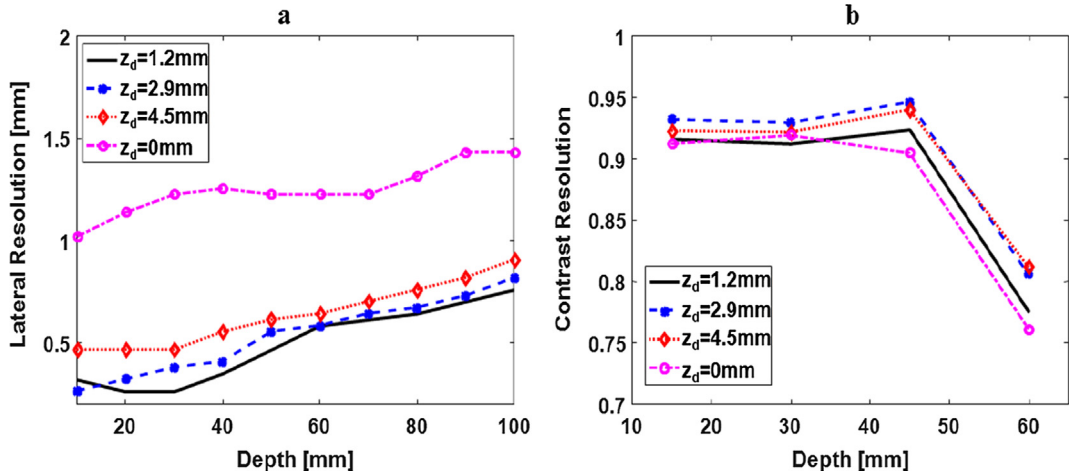

Fig. A1. Plots of the estimated (a) lateral resolution and (b) contrast resolution obtained in simulations when using DB-SAT with different virtual source distances from a transducer array. Here, $z_d = 0$, represents the unfocused beam from the transmit sub-aperture.

References

[1] J.C. Bamber, Image Formation and Image Processing in Ultrasound, Joint Department of Physics, Institute of Cancer Research and The Royal Marsden NHS Trust, Sutton, Surrey, SM2 5PT, UK, 2002, pp. 1–14.
[2] E. Brunner, Ultrasound system considerations and their impact on front- end components, Anal. Dev. (2002) 1–19.
[3] C.B. Burckhardt, An Experimental 2 MHz synthetic aperture sonar system intended for medical use, IEEE Trans. Sonics Ultrason. 21 (1) (1974) 1–6.
[4] J. Camacho, M. Parrilla, C. Fritsch, Phase coherence imaging, IEEE Trans. Ultrason. Ferroelectr. Freq. Control (2009).
[5] K.L. Gammelmark, J.A. Jensen, Multielement synthetic transmit aperture imaging using temporal encoding, IEEE Trans. Med. Imaging 22 (4) (2003) 552–563.
[6] P. Gong, P. Song, S. Chen, Ultrafast synthetic transmit aperture imaging using hadamard-encoded virtual sources with overlapping sub-apertures, IEEE Trans. Med. Imaging 36 (6) (2017) 1372–1381.
[7] F. Guanziroli et al., New generation of High Voltage integrated devices for ultrasound : 16 channels pulser 5 levels with integrated transmit beamformer and 64 independent HV switches, in: IEEE International Ultrasonics Symposium, IUS, 2017.
[8] H. Hasegawa, H. Kanai, High-frame-rate echocardiography using diverging transmit beams and parallel receive beamforming, J. Med. Ultrason. 38 (3) (2011) 129–140.
[9] J.A. Jensen, Field : a program for simulating ultrasound systems field : a program for simulating ultrasound systems, in: 10TH Nordicbaltic Conf. on Biomedical IMG, 34, 1996, pp. 351–353.
[10] J.A. Johnson, et al., Coherent-array imaging using phased subarrays. Part i : basic principles, IEEE Trans. Ultrason. Ferroelectr. Freq. Control 52 (1) (2005) 37–50.
[11] F. Kallel, C.D. Prihoda, J. Ophir, Contrast-transfer efficiency for continuously varying tissue moduli: simulation and phantom validation, Ultrasound Med. Biol. 27 (8) (2001) 1115–1125.
[12] M. Karaman, Atalar, Aykanat, A front-end digital hardware architecture for real-time ultrasound imaging, in: Bilkent Int. Conf. New Trends in Communication, Control and Signal Processing, 1990, pp. 1612–1618.
[13] M. Karaman, Pai-Chi Li, M. O'Donnell, Synthetic aperture imaging for small scale systems, IEEE Trans. Ultrason. Ferroelectr. Freq. Control (1995).
[14] P. Kim et al., Barker-sequence-modulated golay coded excitation technique for ultrasound imaging, in: IEEE International Ultrasonics Symposium, IUS, 2016, pp. 1–4.
[15] P. Li, et al., Adaptive Imaging Using the Generalized, IEEE Trans. Ultrason. Ferroelectr. Freq. Control 50 (2) (2003) 128–141.
[16] G.R. Lockwood, J.R. Talman, S.S. Brunke, Real-Time 3-D ultrasound imaging using sparse synthetic aperture beamforming, IEEE Trans. Ultrason. Ferroelectr. Freq. Control 45 (4) (1998) 980–988.
[17] B. Lokesh, A.K. Thittai, Design of a low cost ultrasound system using diverging beams and synthetic aperture approach : preliminary study, in: Biomedical Imaging (ISBI 2017), IEEE 14th International Symposium, 2017, pp. 1108–1111.
[18] A. Macovski, Ultrasonic imaging using arrays, Proc. IEEE 67 (4) (1979) 484–495.
[19] C.J. Martín-arguedas, et al., An ultrasonic imaging system based on a new SAFT approach and a GPU beamformer, IEEE Trans. Ultrason. Ferroelectr. Freq. Control 59 (7) (2012) 1402–1412.
[20] T.X. Misaridis, et al., Potential of coded excitation in medical ultrasound imaging, Ultrasonics 38 (1) (2000) 183–189.
[21] G. Montaldo, et al., Coherent plane-wave compounding for very high frame rate ultrasonography and transient elastography, IEEE Trans. Ultrason. Ferroelectr. Freq. Control 56 (3) (2009) 489–506.
[22] M. O'Donnell, Coded excitation system for improving the penetration of real-time phased-array imaging systems, IEEE Trans. Ultrason. Ferroelectr. Freq. Control 39 (3) (1992) 341–351.
[23] I. Oguzman, A. Loloee, State of the art IC: transmitter in ultrasound devices, Wireless Des Devel. 17 (8) (2009) 1–8.
[24] C. Papadacci, et al., High-contrast ultrafast imaging of the heart, IEEE Trans. Ultrason. Ferroelectr. Freq. Control 61 (2) (2014) 288–301.
[25] M.S. Patterson, F.S. Foster, The improvement and quantitative assessment of b-mode images produced by an annular array/cone hybrid, Ultrason. Imaging 5 (3) (1983) 195–213.
[26] A. Ponnle, et al., Multi element diverging beam from a linear array transducer for transverse cross sectional imaging of carotid artery : simulations and phantom vessel validation, Jpn. J. Appl. Phys. 50 (7S) (2011) p. 07HF05.
[27] B.R. Reeder, C. Petersen, The AD9271 — A revolutionary solution for portable ultrasound, Analog Dialogue 41 (2007) 40–42.
[28] A. Rodriguez-Molares et al., Axial lobes in coherent plane-wave compounding, in: IEEE International Ultrasonics Symposium, IUS, 2016, November, 2016.
[29] J. Scampini, Overview of ultrasound imaging systems and the electrical components required for main subfunctions, Maxim Integ. 10 (2010) 1–7.
[30] M.E. Schafer, P.A. Lewin, The Influence of front-end hardware on digital ultrasonic imaging, IEEE Trans. Sonics Ultrason. 31 (4) (1984) 295–306.
[31] J.-F. Synnevåg, A. Austeng, S. Holm, Benefits of minimum-variance beamforming in medical ultrasound imaging, IEEE Trans. Ultrason. Ferroelectr. Freq. Control 56 (9) (2009) 1868–1879.
[32] T.L. Szabo, Diagnostic Ultrasound Imaging: Inside Out, Academic Press, 2004.

[33] E. Tiran, et al., Multiplane wave imaging increases signal-to-noise ratio in ultrafast ultrasound imaging, Phys. Med. Biol. 60 (21) (2015) 8549–8566.
[34] G.E. Trahey, L.F. Nock, Synthetic receive aperture imaging with phase correction for motion and for tissue inhomogeneities-Part II: effects of and correction for motion, IEEE Trans. Ultrason. Ferroelectr. Freq. Control 39 (4) (1992) 496–501.
[35] I. Trots, A. Nowicki, M. Lewandowski, Multi-element synthetic transmit aperture in medical ultrasound imaging, Arch. Acoust. 35 (4) (2010) 687–699.
[36] J.T. Ylitalo, H. Ermert, Ultrasound synthetic aperture imaging: monostatic approach, IEEE Trans. Ultrason. Ferroelectr. Freq. Control 41 (3) (1994) 333–339.
[37] Y. Zhang, Y. Guo, W.N. Lee, Ultrafast ultrasound imaging with cascaded dual-polarity waves, IEEE Trans. Med. Imaging 37 (4) (2018) 906–917.